Nanoscale

Monolithic multiscale bilayer inverse opal electrodes for dye-sensitized solar cell applications

Journal Name

ARTICLE

Monolithic multiscale bilayer inverse opal electrodes for dye-sensitized solar cell applications

Jung Woo Lee and Jun Hyuk Moon*

Multilayer structures in which the layers are both electrically and physically connected are critical for use as high-performance electrodes for photovoltaic devices. We present the first multiscale bilayer inverse opal (IO) structures for application as electrodes in dye-sensitized solar cells (DSCs). A bilayer of a mesoscopic IO layer (70 nm pore diameter) and a top macroporous IO layer (215 nm and 250 nm pore diameters) was fabricated as the high-specific-area electrode and the light-harvesting enhancing layer, respectively. The mesoscopic IO layer exhibits a dye-adsorption density that is approximately 4 times greater than that of the macroporous IO structure because of its small pore size. The macroporous IO layer exhibits photonic bandgap reflection in the visible-light wavelength range. We incorporated the bilayer IO electrodes into DSCs and compared the effects of the pore sizes of the macroporous layers on the photocurrent densities of the DSCs. We observed that the bilayer IO electrode DSCs that contained a 250 nm IO layer exhibited photocurrent densities greater than those of 215 nm IO DSCs. This enhanced photocurrent density was achieved because the photonic bandgap(PBG) reflection wavelength matches the wavelength range in which the N719 dye has a small light-absorption coefficient. The fabrication of this structurally homogeneous IO bilayer allows strong contact between the layers, and the resulting bilayer therefore exhibits high photovoltaic performance. We believe that this bilayer structure provides an alternative approach to the development of optimized electrode structures for various devices.

1. Introduction

Dye-sensitized solar cells (DSCs) are regarded as next-generation solar cells because of their high power-conversion efficiency with respect to their simple architecture and low fabrication cost.[1, 2] DSCs have motivated various areas of research, including the development of highly efficient visible-light sensitizing materials, electrode materials and structures, and electrolytes.[3, 4] Among the various components of DSCs, an efficient light-absorbing electrode is essential to attain high efficiency. Multiscale electrodes are widely accepted to represent the optimized electrode architecture for this purpose; a nanoparticulate (NP) TiO$_2$ film, i.e., mesoscopic TiO$_2$ film, have been widely utilized as base electrodes because of their high surface area, and a scattering film consisting of submicrometer particles (i.e., a macroscopic TiO$_2$ film) has been deposited onto this NP film. In the case of liquid-electrolyte DSCs, a record efficiency has been achieved using this type of bilayer electrode with a 5-10 μm thick scattering film on a 10-15 μm thick NP film.[3-5]

Recently, further engineering of TiO$_2$ electrodes has been undertaken to further enhance their efficiency, primarily by ameliorating the charge diffusion across the TiO$_2$ film to the charge-collecting substrate (i.e., FTO). TiO$_2$ nanostructures such as nanotubes, nanorods, nanofibers, and inverse opals (IOs) have been adopted and have yielded promising results, including enhanced charge diffusion or facile electrolyte infiltration.[6-12] Notably, however, these materials have been used only as substitutes for either the nanoparticulate TiO$_2$ film or the scattering film. Multiscale electrodes based on these materials has not been demonstrated yet. This may be attributed to the difficulty of fabricating these materials in a broad size range. In the case of IO-based electrodes, IO structures with a pore size on the order of 100 nm or up to 1 μm have been utilized directly as porous electrodes. Specifically, because of the relatively low internal surface area of this macroporous IO structure, additional surface modification such as nanoparticle decoration have been often introduced to enhance the specific area of the electrode.[13, 14] Alternatively, IO structures whose cavity size is comparable to the light wavelength (i.e., approximately 200-300 nm) exhibits photonic bandgap (PBG) properties in the visible-light range, which have been used as the second scattering layer on conventional NP electrodes.[10, 15, 16] Such an IO layer serves as an efficient light reflector (light

reflection back toward the electrode), thereby enhancing the light-harvesting efficiency.

In this study, we present the first multiscale bilayer IO structures for application as electrodes in dye-sensitized solar cells (DSCs). We fabricated a sub-100 nm mesoscopic IO layer and a submicrometer macroscopic IO layer on top. Thus, the mesoscopic porous IO structures, serving as high-surface-area electrodes, were combined with macroporous IO scattering films with visible PBGs. First of all, the mesoscopic IO layer exhibits a dye-adsorption density that is approximately 4 times greater than that of the macroporous IO structure because of its small pore size. Second, the fabrication of this structurally homogeneous IO bilayer allows strong contact between the layers, and the resulting bilayer therefore exhibits high photovoltaic performance. Previous results have reported difficulty in fabricating an intact film of IO structure on the NP electrode, resulting in only marginal efficiency enhancement.[10] Specifically, we prepared two different macroporous top layers with PBGs at wavelengths of approximately 560 and 670 nm. We clearly observed that more photocurrent density was achieved for the DSCs with the top layer exhibiting 670 nm bandgap reflection, which was because the PBG reflection wavelength matches the wavelength range in which the N719 dye has a small light-absorption coefficient. We believe that this bilayer structure provides an alternative approach to the development of optimized electrode structures for various photoelectrochemical or electrochemical devices.

2. Experimental

Preparation of the bilayer IO TiO2 films.

Fluorine-doped tin oxide (FTO) glass was used as a substrate. Polystyrene (PS) particles with a diameter of 99 nm were purchased from the Bangs Lab. PS particles with a diameter of 230 nm or 260 nm were obtained through emulsifier-free emulsion polymerization using styrene monomer and potassium persulfate initiator. Colloidal-crystal layers of 99 nm PS particles and 230 nm or 260 nm PS particles were coated onto the FTO substrate using the plate-sliding approach.[17] In brief, two parallel substrates of FTO and glass substrate filled with PS dispersion were prepared. During the sliding of the glass substrate, colloidal particles were deposited at the end of the substrate. By changing the coating rate, we controlled the thicknesses of the sub-100 nm colloidal crystals and the macroscale colloidal crystals in the ranges of 1-5 μm and 1-7 μm, respectively. The typical coating rate was approximately 1.15 cm^2/min. Meanwhile, TiO$_2$ deposition was performed using atomic layer deposition. Titanium tetrachloride and deionized water were used as precursors and were sequentially introduced into the reactor using N$_2$ gas. A fill pressure of 0.55 Torr, an exposure time of 15 s and a purge time of 17 s were used throughout the deposition for both TiCl$_4$ and H$_2$O. The thickness of the deposited TiO$_2$ was controlled by adjusting the number of cycles of precursor exposure; the typical deposition

rate was approximately 0.13 nm/cycle. Subsequently, the TiO$_2$-deposited PS colloidal crystals were heated to 500 °C for 2 h in air to remove the PS templates.

Assembly of DSCs

Each sample was calcined at 300 °C prior to dye sensitization. The area of the IO TiO$_2$ film was controlled via scraping to be approximately 9 mm^2. N719 dye (obtained from Dyesol Inc. and used without any further purification) was utilized as the sensitizer for the bilayer TiO$_2$ films; the films were soaked in a 0.5 mM N719 (Dyesol) ethanol solution overnight. A Pt counter electrode was prepared by coating a 0.7 mM H$_2$PtCl$_6$ solution in anhydrous ethanol onto an FTO substrate and subsequently subjecting the coated substrate to heat treatment. The bilayer TiO$_2$ IO-coated FTO substrate and the counter electrode were then assembled; the gap between the two electrodes was fixed using a 60 μm thick polymeric film (Surlyn, DuPont). Finally, the electrolyte solution was injected into the gap; the electrolyte solution was prepared by mixing 0.05 M LiI (Sigma-Aldrich), 0.1 M guanidine thiocyanate (GSCN) (Wako), 0.03 M I$_2$ (Yakuri), 0.5 M 4-*tert*-butylpyridine (Aldrich), and 0.7 M 1-butyl-3-methylimidazolium iodide (BMII) (Sigma-Aldrich) in a solution containing acetonitrile (Aldrich) and valeronitrile (85:15 v/v).

Characterization.

Scanning electron microscopy (SEM) images were obtained using a field-emission scanning electron microscopy (Hitachi S-4700). Absorption spectra were recorded using a UV-Vis spectrophotometer (UV-2550, Shimadzu). Raman spectra were recorded using micro-Raman spectroscopy (Tokyo Instruments, Nanofinder) at an excitation wavelength of 487.55 nm. The amount of adsorbed dye molecules was determined spectrophotometrically. Briefly, the dyes on a known TiO$_2$ film area were detached in a 0.1M NaOH solution. The absorption intensity of the dye solution was estimated by UV-vis spectrophotometer and then, converted to concentration of adsorbed dye molecules. The *J*–*V* characteristics of the DSSCs were measured using a SourceMeter (Keithley Instruments) under simulated solar light, which was provided by a solar simulator (1000 W Xe lamp with an AM 1.5G filter). The light intensity was adjusted to 100 mW cm^{-2} using a Si reference cell (BS-520, Bunko-Keiki). The incident photon-to-current conversion efficiency (IPCE) was estimated using a 300 W Xe light source (Oriel) with a monochromator operated in DC mode. The incident light intensity was estimated using a photodiode detector (calibrated silicon detector, Newport). The charge-transport properties were measured via intensity-modulated photocurrent spectroscopy (IMPS) and intensity-modulated voltage spectroscopy (IMVS) using a frequency response analyzer (XPOT, Zahner).
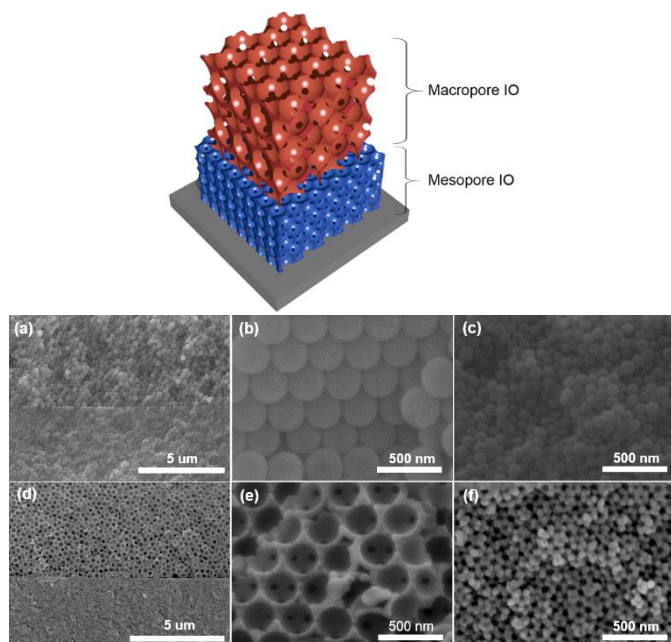
3. Results and Discussion

Fig. 1. Schematic image of the bilayer inverse opal (IO) layer. Cross-sectional SEM images of (a) bilayer colloidal crystals and (d) their inverted structure as well as magnified SEM images of the (b,e) top layer and (c,f) bottom layer.

The monolithic multiscale bilayer IOs as described in **Figure 1** were prepared using PS colloidal-crystal bilayer templates. A colloidal solution in which 99 nm diameter PS was dispersed was utilized to obtain the mesoscopic IO structures and to deposit them onto the substrate; 230 nm or 260 nm PS dispersions were subsequently deposited on top of these mesoscopic structures. **Figure 1a** clearly displays a cross-sectional image of a multiscale bilayer of colloidal crystals; the thicknesses of the top and bottom colloidal crystals was 8 μm and 7 μm, respectively. **Figures 1b and 1c** present magnified images of the top and bottom layers of colloidal crystals.

The atomic layer deposition (ALD) technique was used to deposit TiO_2 coating into the cavities of these colloidal crystals. The TiO_2 layer was formed through alternating exposure of the colloidal crystals to titanium tetrachloride and water vapor as precursors. We controlled the thickness of the TiO_2 layer by adjusting the number of exposure cycles; here, a TiO_2 layer with a thickness of 25 nm was typically obtained. **Figure 1d** presents a cross-sectional image of a multiscale bilayer of IOs that we obtained by removing the PS colloidal-crystal film. **Figures 1e and 1f** present magnified images of the top and bottom IO films, respectively. The bottom mesoscopic IO layers contain pores approximately 70 nm in diameter. The top macroporous IO film prepared from the 260 nm PS samples exhibits pore diameter of 250 nm. The deposited TiO_2 was characterized using Raman spectroscopy, as shown in **Figure S1**. The peaks were observed to correspond to the anatase phase of TiO_2 materials.

We indirectly estimated the surface areas of the bilayer inverse opal TiO_2 films by characterizing their loading capacities (adsorbed dye amount per TiO_2 film area) for sensitizing-dye molecules (N719). The dye-loading capacity directly affects the photocurrent density and thus the efficiency of DSCs. The adsorption density of the bilayer IO structure was estimated to be 0.118 μmol cm^{-2}. Notably, the IO structure with 70 nm pores is the primary contributor to this adsorption density; the mesoscopic IO films exhibit an adsorption density of 0.093 μmol cm^{-2}.
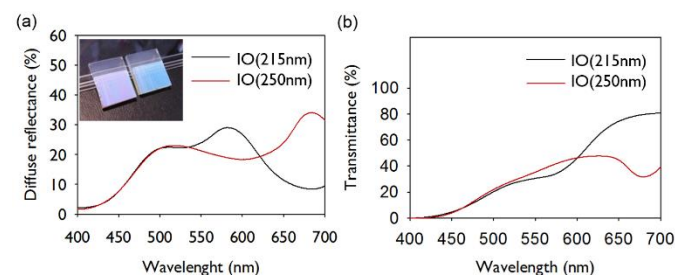

Fig. 2. (a) UV-Vis reflectances of the macroporous IO films with pore diameters of 215 nm and 250 nm. (b) Transmittance spectra of the macroporous IO films. The inset photographs are 215 nm (left) and 250 nm (right) macroporous IO films.

The UV-Vis spectra of the bilayer IO TiO_2 films were characterized, as shown in **Figure 2**. The inset photographs of the films clearly display their opalescent colors, which arise from the PBG feature of the long-ranged, highly ordered macropore arrays of the IO structures. As shown in **Figure 2a**, the UV-Vis reflectances of these films exhibit peaks at 580 nm and 680 nm for the IO films with 215 nm and 250 nm cavities, respectively. These measurements were performed using macroporous IO films soaked with electrolyte solution to simulate the reflection in the assembled DSCs. Meanwhile, the shoulder at approximately 500 nm in each reflectance spectrum is attributed to absorption by the electrolyte solution. In **Figure 2b**, each transmittance spectrum exhibits a dip that corresponds to the reflectance peak. The reflectance peaks (and the transmission dips) in the UV-Vis spectra that arise from the PBG can be simply estimated using the Bragg equation. The Bragg peak, and thus the PBG wavelength in the direction normal to the surface of the IO film (the gamma-L direction), can be described by

$$\lambda = 2\, n_{eff} \sqrt{\tfrac{2}{3}}\, D$$

$$n_{eff} = \sqrt{f\, n_{TiO_2}^2 + (1-f)\, n_{liquid}^2}$$

where λ is the PBG wavelength, D is the cavity diameter, f is the TiO_2 volume fraction, and n is the refractive index. In the case of the 215 nm cavity IO films, λ was calculated to be 584 nm using $n(TiO_2) = 2.4$, $n(liquid) = 1.35$ (effective refractive index of acetonitrile and valeronitrile mixture), and $f = 0.24$. The λ of 250 nm cavity IO films was calculated to be 680 nm. This calculated wavelengths are similar to the spectral absorption peak wavelength.
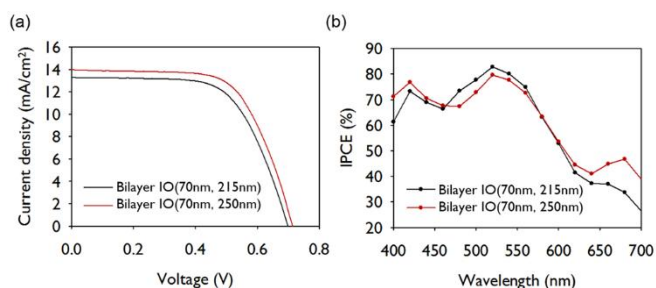
Fig. 3. (a) J–V curves and (b) IPCE spectra of DSCs containing bilayer TiO2 IO electrode films.

Table 1. Photovoltaic parameters and photon-to-current conversion efficiencies of DSCs containing bilayer IO electrode films.

Film type	V_{oc} [V]	J_{sc} [mA/cm^2]	FF	η [%]
Bilayer (70nm,215nm,)	0.70	13.29	0.64	5.93
Bilayer (70nm,250nm)	0.71	13.98	0.65	6.46

Finally, we applied the multiscale bilayer TiO$_2$ IO films as photoelectrodes in DSCs. The current–voltage (J–V) characteristics of the DSCs were measured under AM 1.5 illumination at 100 mW cm^{-2}. **Figure 3a** presents the J–V curves for the DSCs, and **Table 1** lists the J–V parameters extracted from the J–V curves, including the J_{sc}, V_{oc}, and FF, and the overall conversion efficiency (η), calculated as $J_{sc} \times V_{oc} \times FF$ / (100 mW cm^{-2}). Here, the data were obtained as the average of 4 cells each. First of all, the J_{sc} of a DSC fabricated with only the mesoscopic bottom layer (i.e., without the macroporous top IO layer) was approximately 10.04 mA/cm^2 (see **Figure S2**). Thus, the photocurrent and efficiency enhancement achieved with the addition of the top IO layer was as high as approximately 40%, which is also superior to previously achieved result.[10, 18] This achievement may be attributed to the fabrication of a monolithic electrode structure. Previously, approaches using photonic-crystal top layers have encountered difficulties in achieving strong physical contact with the bottom layer.[10] In this case, the top layer may be served only as a light reflector, not as an electrically conducting electrode. Here, the homogeneous PS opal templates that were applied to produce mesoscopic pores and macropores assisted in overcoming this limitation.

Meanwhile, when the two types of bilayer electrode DSCs are compared, the bilayers comprising 250 nm macroporous IO films exhibit J_{sc} that is higher by approximately 5%, leading to higher efficiency. We controlled the top macroporous IO layers to be of very similar thicknesses. Thus, the dye adsorption amount should be higher for the 215 nm IO layer than for the 250 nm IO layer because of its smaller pore diameter. Therefore, the higher photocurrent harvesting of the 250 nm IO layer implies that some other factor is affecting the light harvesting. To reveal the effects of macroporous IO layers with different pore diameters, the IPCEs of the DSCs containing the

two different types of top layers are compared in **Figure 3b**. The most apparent difference is that the 250 nm IO layer exhibits a higher IPCE value at a wavelength of approximately 680 nm. Notably, the 250 nm IO layer possesses a bandgap wavelength in this wavelength range. Thus, the higher J_{sc} of the 250 nm IO layer DSCs is attributable to the higher light-harvesting efficiency facilitated by the strong PBG reflection at this wavelength, as shown in **Figure 2**.[19] However, no apparent increase in the IPCE value of the 215 nm IO layer DSCs is observed at a wavelength of approximately 580 nm, where the 215 nm IO possesses a PBG. This lack of increase is attributed to the fact that the N719 dye exhibits a high molar absorption coefficient at 580 nm; the molar extinction coefficient of N719 at 580 nm is 6 times higher than its coefficient at 680 nm; i.e., the light absorption by N719 at this wavelength is sufficiently high to negate the light-harvesting enhancement provided by the PBG reflection.
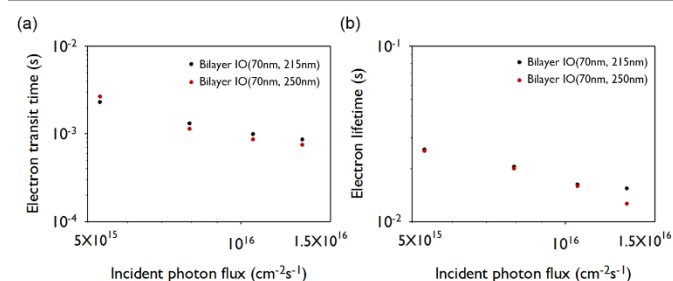

Fig. 4. (a) The electron transport times and (b) electron lifetimes for bilayer TiO$_2$ IO electrode DSCs.

Meanwhile, the J_{sc} was also affected by the efficiencies of charge injection (N719 to the TiO$_2$ conduction band) and charge collection (diffusion through the TiO$_2$ to the substrate) as well as light harvesting. In this case, we can expect that the injection efficiencies should be the same for all investigated electrodes because the injection depends on the energy-level difference between N719 and TiO$_2$ materials. Meanwhile, the collection efficiency can be determined from the ratio of the electron transit time to the electron lifetime. The IMVS and IMPS of the DSCs containing the two different types of top layers were measured and characterized, as shown in **Figure 4**. The charge transport time (τ_c) and charge recombination lifetime (τ_r) were obtained from the angular-frequency minima in the IMPS Nyquist plot ($\tau_c = 1/2\pi f$) and the IMVS Nyquist plot ($\tau_r = 1/2\pi f$), respectively, where f is the frequency that corresponds to the minimum imaginary component. [20, 21] The collection efficiency (η_{cc}) was determined from the ratio of these characteristic times, i.e., $\eta_{cc} = 1 - (\tau_c/\tau_r)$. **Figure S3** presents the Nyquist plots of the IMPS and IMVS responses at the largest photon flux, and **Figure 4** displays the transit times and lifetimes at various incident photon fluxes. These characteristic times have similar values; therefore, the collection efficiencies of DSCs containing the two different types of top layers are also similar. Thus, the results of comparing the charge-collection and injection efficiencies confirm that the larger photocurrent density observed for the

250 nm IO DSCs is attributed to the light-harvesting enhancement provided by the PBG.

4. Conclusion

In summary, we report the first realization of a bilayer consisting of a high-specific-area electrode and a scattering top layer using multiscale IO structures. An IO layer with 70 nm diameter pores and a TiO_2 IO layer with 215 nm or 250 nm diameter pores were obtained using different sizes of PS colloidal-crystal templates, and these layers were used as the highly porous electrode and the top layer, respectively. We observed that this structurally homogeneous fabrication method enabled the establishment of strong physical contact between the layers, which should be beneficial to the electrical contact between the layers required for electrode applications. The bilayer IO structure exhibited a high dye-adsorption density per film area, which was primarily attributable to the contribution of the mesoscopic IO films. The top macroporous IO layer displayed a PBG (gamma-L gap) at approximately 580 nm in the case of the 215 nm IO film or 680 nm in the case of the 250 nm IO film, thereby satisfying the Bragg condition. These multiscale bilayer TiO_2 layers were applied as electrodes in DSCs. In these DSCs, we achieved a maximum photocurrent density of 13.98 mA/cm^2 and an efficiency of 6.46%. Meanwhile, the photocurrent density of the DSCs that contained 250 nm IO layers was 5% higher than that of the 215 nm IO layer DSCs. In IPCE measurements under visible light, the 250 nm IO DSCs exhibited an IPCE value at the wavelength corresponding to the PBG (i.e., 680 nm) greater than that of the 215 nm IO layer DSCs. However, the 215 nm IO layer did not yield a higher IPCE value at its bandgap wavelength; this lack of enhancement was explained in terms of the much greater absorptivity of the N719 dye at this wavelength. Moreover, the charge-collection efficiency was similar for both electrodes; this observation also confirms that the photocurrent enhancement of the DSCs containing 250 nm IO layers arose from the light-harvesting enhancement provided by the PBG. We are currently optimizing each layer thickness in the bilayer IO structure or introducing the sensitization with high extinction coefficient molecules or particles to enhance the DSC efficiency. We believe the monolithic multiscale IO layers may be also useful for ranging from other photoelectrochemical applications to catalysts or separation membranes.

Notes and references

Department of Chemical Biomolecular Engineering, Sogang University, 35 Baekbeom-ro, Mapo-gu, Seoul 121-742, Korea. E-mail: junhyuk@sogang.ac.kr; Fax: +82 2 711 0439; Tel: +82 2 705 8921

1. B. Oregan and M. Gratzel, *Nature*, 1991, **353**, 737-740.
2. B. E. Hardin, H. J. Snaith and M. D. McGehee, *Nat. Photon.*, 2012, **6**, 162-169.
3. A. Hagfeldt, G. Boschloo, L. C. Sun, L. Kloo and H. Pettersson, *Chem. Rev.*, 2010, **110**, 6595-6663.
4. M. Grätzel, *Acc. Chem. Res.*, 2009, **42**, 1788-1798.
5. Y. Chiba, A. Islam, Y. Watanabe, R. Komiya, N. Koide and L. Y. Han, *Jap. J. Appl. Phys.*, 2006, **45**, L638-L640.
6. Q. Zhang and G. Cao, *Nano Today*, 2011, **6**, 91-109.
7. J. R. Jennings, A. Ghicov, L. M. Peter, P. Schmuki and A. B. Walker, *J. Am. Chem. Soc.*, 2008, **130**, 13364-13372.
8. K. Zhu, N. R. Neale, A. Miedaner and A. J. Frank, *Nano Lett.*, 2007, **7**, 69-74.
9. N. Tetreault, E. Horvath, T. Moehl, J. Brillet, R. Smajda, S. Bungener, N. Cai, P. Wang, S. M. Zakeeruddin, L. Forro, A. Magrez and M. Graetzel, *ACS Nano*, 2010, **4**, 7644-7650.
10. S. Guldin, S. Huttner, M. Kolle, M. E. Welland, P. Muller-Buschbaum, R. H. Friend, U. Steiner and N. Tetreault, *Nano Lett.*, 2010, **10**, 2303-2309.
11. N. Tetreault, E. Arsenault, L.-P. Heiniger, N. Soheilnia, J. Brillet, T. Moehl, S. Zakeeruddin, G. A. Ozin and M. Graetzel, *Nano Lett.*, 2011, **11**, 4579-4584.
12. L. N. Quan, Y. H. Jang, K. A. Stoerzinger, K. J. May, Y. J. Jang, S. T. Kochuveedu, Y. Shao-Horn and D. H. Kim, *Phys. Chem. Chem. Phys.*, 2014, **16**, 9023-9030.
13. H. N. Kim, H. Yoo and J. H. Moon, *Nanoscale*, 2013, **5**, 4200-4204.
14. J. H. Shin and J. H. Moon, *Langmuir*, 2011, **27**, 6311-6315.
15. S. Colodrero, A. Mihi, J. A. Anta, M. Ocana and H. Miguez, *J. Phys. Chem. C*, 2009, **113**, 1150-1154.
16. N. Tetreault and M. Graetzel, *Energ. Environ. Sci.*, 2012, **5**, 8506-8516.
17. Y. G. Seo, K. Woo, J. Kim, H. Lee and W. Lee, *Adv. Funct. Mater.*, 2011, **21**, 3094-3103.
18. A. Mihi, C. Zhang and P. V. Braun, *Angew. Chem. Inter. Ed.*, 2011, **50**, 5712-5715.
19. Y. H. Jang and D. H. Kim, *Nanoscale*, 2014, **6**, 4204-4210.
20. J. Bisquert, F. Fabregat-Santiago, I. Mora-Sero, G. Garcia-Belmonte and S. Gimenez, *J. Phys. Chem. C*, 2009, **113**, 17278-17290.
21. S. Nakade, Y. Saito, W. Kubo, T. Kitamura, Y. Wada and S. Yanagida, *J. Phys. Chem. B*, 2003, **107**, 8607-8611.